PNAS RESEARCH ARTICLE | CHEMISTRY

Enhancing ion selectivity by tuning solvation abilities of covalent-organic-framework membranes

Qing-Wei Meng[a], Xincheng Zhu[a], Weipeng Xian[a], Sai Wang[a], Zhengqing Zhang[b,1], Liping Zheng[c], Zhifeng Dai[c], Hong Yin[a], Shengqian Ma[d], and Qi Sun[a,1]

Edited by Omar K. Farha, Northwestern University, Evanston, IL; received September 28, 2023; accepted January 2, 2024 by Editorial Board Member Chad A. Mirkin

Understanding the molecular-level mechanisms involved in transmembrane ion selectivity is essential for optimizing membrane separation performance. In this study, we reveal our observations regarding the transmembrane behavior of Li^+ and Mg^{2+} ions as a response to the changing pore solvation abilities of the covalent-organic-framework (COF) membranes. These abilities were manipulated by adjusting the lengths of the oligoether segments attached to the pore channels. Through comparative experiments, we were able to unravel the relationships between pore solvation ability and various ion transport properties, such as partitioning, conduction, and selectivity. We also emphasize the significance of the competition between Li^+ and Mg^{2+} with the solvating segments in modulating selectivity. We found that increasing the length of the oligoether chain facilitated ion transport; however, it was the COF membrane with oligoether chains containing two ethylene oxide units that exhibited the most pronounced discrepancy in transmembrane energy barrier between Li^+ and Mg^{2+}, resulting in the highest separation factor among all the evaluated membranes. Remarkably, under electro-driven binary-salt conditions, this specific COF membrane achieved an exceptional Li^+/Mg^{2+} selectivity of up to 1352, making it one of the most effective membranes available for Li^+/Mg^{2+} separation. The insights gained from this study significantly contribute to advancing our understanding of selective ion transport within confined nanospaces and provide valuable design principles for developing highly selective COF membranes.

membrane separation | covalent organic framework | solvation ability | ion separation | facilitated transport

Lithium has been recognized as "white gold" owing to its indispensable role in portable electronic devices and electric vehicles (1). In a bid to ensure a consistent lithium supply, there's been substantial interest in extracting it from unconventional aqueous sources, specifically salt lakes (2–5). One significant hurdle in this process, however, is the efficient separation of Li^+ from Mg^{2+} given their closely related chemical properties (6). Nature provides an inspirational glimpse into the structural and chemical features needed for membranes in ion screening processes (7–11). The exceptional selectivity demonstrated by biological ion channels is thought to result from the solvation/coordination interactions between the target analyte and the membrane pore channel (12). As such, replicating this level of selectivity in synthetic membranes necessitates meticulous control over the pore's solvation/coordination capabilities. While there has been research focusing on size sieving and Donnan exclusion in synthetic membranes, the exploration of this selectivity mechanism remains relatively sparse. Therefore, a deepened understanding and application of the solvation/coordination properties of membranes represent vital research directions for future advancements in separating Li^+ and Mg^{2+} ions.

In our recent study, we utilized the concept of polymer electrolytes, commonly employed for Li^+ conduction, to customize the interactions between ions and membranes. Our approach involved embedding lithiophilic oligoether groups into the pore channels of a covalent-organic-framework (COF) membrane. This incorporation of oligoethers allowed us to achieve selectivity between Li^+ and Mg^{2+} with an impressive separation factor of up to 64 (13). Primarily, the selectivity of the membrane is dependent on the cumulative energy barrier, which is influenced by the partitioning and diffusion of ions through the membrane pore channels (14–16). Considering that oligoethers with various numbers of ethylene oxide (EO) units have different solvation capabilities (the EO unit can act as substitutes for the water oxygen atoms that surround the ions) and flexibility, these oligoether chains can potentially impact the barriers to ion transport within the membrane (17–21). Therefore, by adjusting the length of oligoether units within the pore channel, we may be able to optimize the energy differences between ions crossing the membrane, leading to enhanced separation performance (Fig. 1).

Significance

Lithium plays a pivotal role in clean energy. As demand soars, there's a pressing need for advanced isolation methods. Current membranes, while promising, often fall short in achieving optimal Li^+ selectivity. Tackling this problem, we present a series of covalent-organic-framework membranes integrated with diverse oligoether chains. This incorporation markedly boosts the transport activity and selectivity of LiCl over $MgCl_2$. By adjusting the lengths of the oligoether chains, we can finely tune the transmembrane energy disparities for various ions, resulting in vastly improved separation capabilities. Particularly noteworthy is the membrane that incorporates oligoether chains consisting of two ethylene oxide units, as it achieves an exceptional Li^+/Mg^{2+} selectivity of 1352. This advancement signifies a crucial step in membrane-based ion separation technology.

Author contributions: Q.S. designed research; Q.-W.M., X.Z., W.X., S.W., Z.Z., and L.Z. performed research; Q.-W.M. analyzed data; Z.Z. conducted the theoretical simulation; H.Y. and S.M. provide valuable suggestion; and Q.-W.M., X.Z., W.X., Z.Z., Z.D., H.Y., S.M., and Q.S. wrote the paper.

The authors declare no competing interest.

This article is a PNAS Direct Submission. O.K.F. is a guest editor invited by the Editorial Board.

[1]To whom correspondence may be addressed. Email: zhangzhengqing@tiangong.edu.cn or sunqichs@zju.edu.cn.

This article contains supporting information online at https://www.pnas.org/lookup/suppl/doi:10.1073/pnas.2316716121/-/DCSupplemental.

Published February 13, 2024.

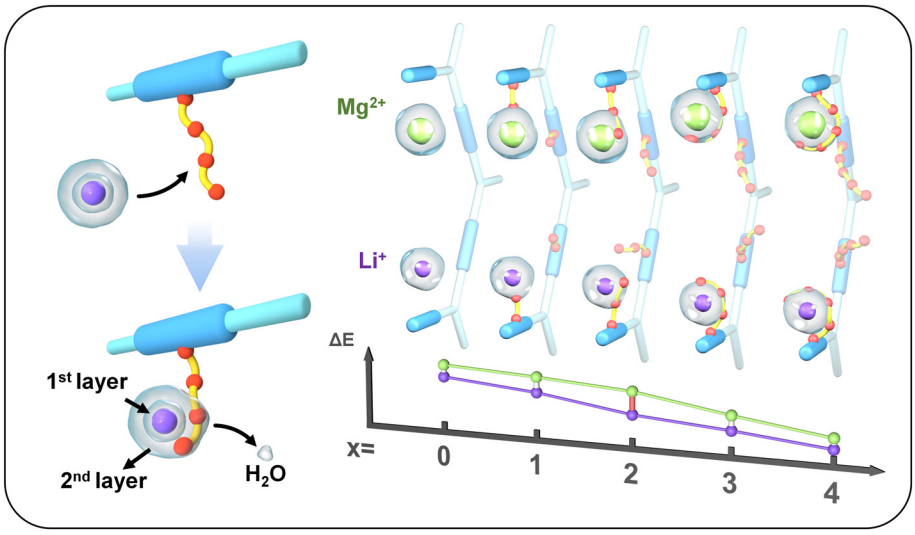

Fig. 1. Conceptual diagram of engineering the solvation ability of COF membranes by tuning the length of oligoether chains lined in pore channels to optimize the ion separation performance.

In this study, we conducted research on the fabrication of oligoether-functionalized COF membranes based on the isoreticular principle. These COF membranes were designed to contain oligoether segments with varying numbers of EO units, which resulted in differing solvation abilities while maintaining the same lattice structure. The core objective of our exploration was to gain an understanding of how the oligoether chain length influences energy barriers for ion partitioning into the pores and their subsequent diffusion through pore channels. Our findings indicate that the inclusion of oligoethers in COF membranes amplifies Li^+ conductivity and boosts the separation efficiency between Li^+ and Mg^{2+} ions, in contrast to their oligoether-free counterparts. Notably, of all the membrane variants tested, the COF membrane with two EO units exhibited a pronounced energy disparity between Li^+ and Mg^{2+}. This translated to a remarkable Li^+/Mg^{2+} selectivity, reaching up to 1352 under electro-driven binary-salt conditions. This finding holds considerable importance, shedding light on crafting highly selective COF membranes with superior ion conduction capabilities.

Results

Design Principles of Li^+/Mg^{2+}-Selective Membranes. To fabricate membranes with varying numbers of EO units, triformylphloroglucinol (Tp) was used to pair hydrazide monomers with different numbers of EO units on the linkers. These membranes were designated as COF-EO_x, where x represents the number of EO units. COFs built from Tp are known for their chemical stability and compatibility with a wide range of hydrazide derivatives. This allowed us to focus on the relationship between the pore structure and selectivity, ensuring highly accurate comparative studies (22–26) (Fig. 2).

To investigate the transmembrane behavior of Li^+ and Mg^{2+} ions across COF layers containing oligoether moieties of varying lengths, we performed molecular dynamics (MD) simulations. These COF structures were based on the isostructural analog COF-EO_0, constructed from Tp and terephthalohydrazide. To calculate the potential of mean force (PMF) profiles, we simulated the passage of ions through the COF-EO_x layers along the [100] direction (eclipsed stacking). Our results demonstrated that the transmembrane free-energy barriers of Li^+ and Mg^{2+} initially decrease and then plateau as the number of EO units increases. This observation indicates the significant role of the oligoether chains in facilitating ion transport. Interestingly, the COF-EO_4 membrane, which contains the longest oligoether chain, did not exhibit the largest difference in transmembrane barriers between Li^+ and Mg^{2+} ions. Conversely, the COF-EO_2 membrane displayed the highest transmembrane energy difference among all the investigated membranes (Fig. 3*A* and *SI Appendix*, Fig. S1). These intriguing findings suggest that oligoethers can effectively regulate the pore environments of COF membranes and optimize their performance in separating Li^+ and Mg^{2+}.

Membrane Preparation and Characterization. Encouraged by the simulation results, we focused on experimentally determinating the aforementioned correlations. To increase the operability, we synthesized COF active layers on polyacrylonitrile (PAN) ultrafiltration membranes with a molecular weight cut-off of 50,000 Da via liquid–liquid interfacial condensation. In this process, an aqueous acetic acid solution of hydrazides and a mesitylene-ethyl acetate-Tp solution were placed on either side of the PAN (*SI Appendix*, Fig. S2). We examined the formation of the COFs using Fourier transform infrared (FT-IR) spectroscopy and solid-state ^{13}C NMR spectroscopy. In the FT-IR spectrum, the bands corresponding to the N–H (3,306 to 3,384 cm^{-1}) and C=O (1,640 cm^{-1}) stretching vibrations, which are characteristic of hydrazide monomers and Tp, respectively, disappeared (*SI Appendix*, Fig. S3). This was further confirmed by the concomitant appearance of a ß-ketoenamine carbonyl stretching band at 1,668 cm^{-1}. Moreover, the solid-state ^{13}C NMR spectrum showed a signal at 191.1 ppm, which could be attributed to the transformation of the enol form to the keto tautomer (22) (*SI Appendix*, Fig. S4). SEM (Scanning electron microscopy) images revealed continuous COF layers on the PAN layer with thicknesses ranging from 142 to 156 nm for COF-EO_x/PAN (*SI Appendix*, Figs. S5–S10). We evaluated the crystallinity of all the COF-EO_x/PAN membranes using powder X-ray diffraction (PXRD). Although the active COF layers were thin, their diffraction peaks could still be observed, indicating high crystallinity (*SI Appendix*, Fig. S11). Additionally, grazing-incidence wide-angle X-ray scattering (GIWAXS) analysis was conducted on the COF-EO_2/PAN membrane, which confirmed the crystallinity of the COF layer on the PAN support. However, the GIWAXS pattern revealed no preferential orientation in the in-plane direction, as evidenced by a circular pattern at

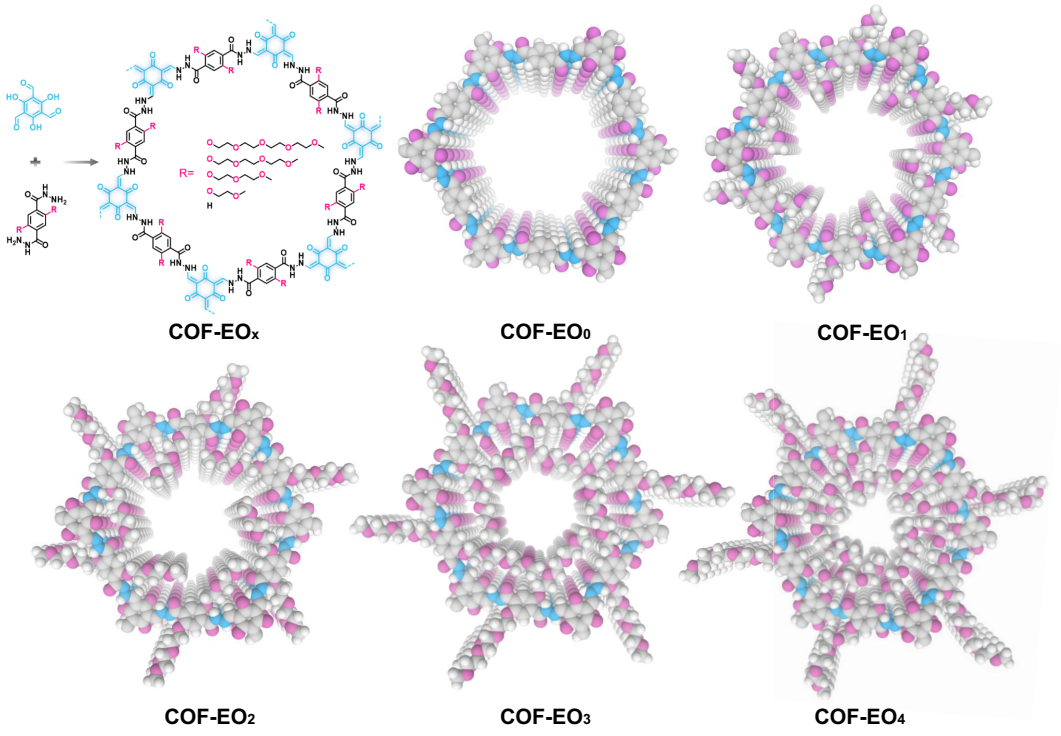

Fig. 2. Chemical structures of COF-EO$_x$.

Qz = 0 (*SI Appendix*, Fig. S12). To identify the COF structures, we dissolved the PAN layer in dimethylformamide to highlight the diffraction peaks of the COFs. Free-standing COF membranes were synthesized using the same procedures as those for the corresponding composite membranes. The resulting PXRD patterns mirrored each other, indicating isostructural features (*SI Appendix*, Figs. S13 and S14). To elucidate the COF structures, we compared them to the analogous COF-EO$_0$ (*SI Appendix*, Fig. S15). The experimental data were consistent with the simulated PXRD pattern of COF-EO$_0$ with an eclipsed structure, verifying that the overall lattice structure was not perturbed by varying the length of the oligoether chains on the linkers (*SI Appendix*, Table S1). The crystallinity of the COF membranes was further verified by transmission electron microscopy (TEM), which revealed clear lattice fringes (*SI Appendix*, Fig. S16).

Evaluation of Membrane Pore Size. Subsequently, we assessed the compactness of the synthesized COF-EO$_x$/PAN membranes by measuring the transmembrane conductance of tetramethyl, tetraethyl, tetrapropyl, tetrabutyl, and tetrapentylammonium chloride solutions. Our measurements revealed that the transmembrane mobility of the cations (α_m) decreased compared to their corresponding bulk values (α_{bulk}), and their discrepancies in mobility increased as the size of the cations increased (27, 28) (Fig. 3*B*). Using the hydrodynamic equation, $\alpha_m / \alpha_{bulk} = c(1 - D_H/D)^2$, where α_m and α_{bulk} are normalized using the mobilities of Cl^- as a reference, c is a constant coefficient, and D_H and D are the diameter of the hydrated cations and membrane pore size, respectively, the pore sizes of the COF-EO$_x$/PAN membranes were estimated to be 2.86, 2.51, 2.13, 1.98, and 1.82 nm, for COF-EO$_0$/PAN, COF-EO$_1$/PAN, COF-EO$_2$/PAN, COF-EO$_3$/PAN, and COF-EO$_4$/PAN, respectively

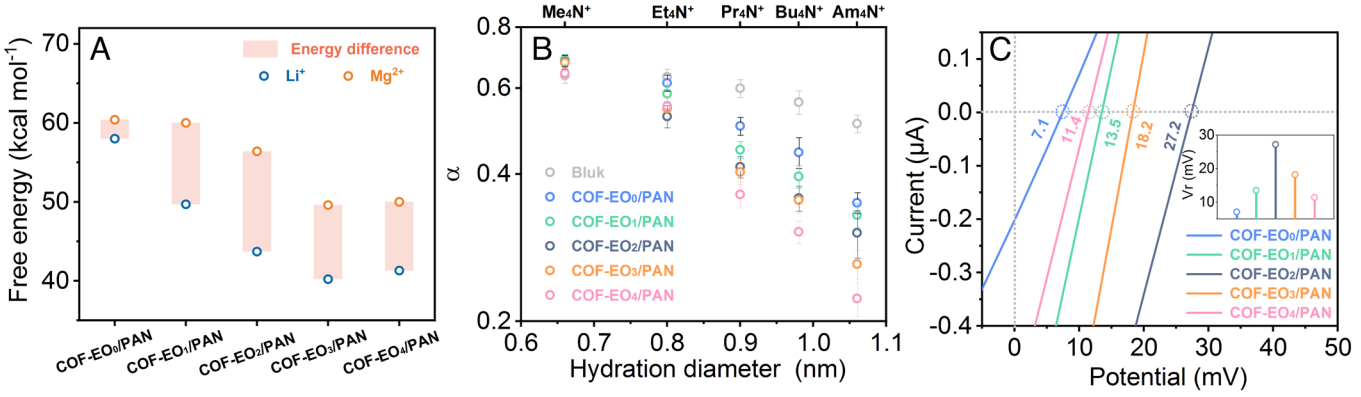

Fig. 3. Investigation of transmembrane ion behavior. (*A*) Plots of transmembrane free-energy barriers for Li^+ and Mg^{2+} ions across COF-EO$_x$, derived from the PMF profiles (*SI Appendix*, Fig. S1), (*B*) plots of the relative mobility of tetraalkylammonium cations to Cl^- anion across the COF-EO$_x$/PAN membranes and in bulk versus the radius of tetraalkylammonium cations, (*C*) I–V plots for COF-EO$_x$/PAN recorded under asymmetrical salt solutions with the *cis* and *trans* sides being filled with 0.05 M $MgCl_2$ and 0.1 M LiCl aqueous solutions, respectively (*Inset*: summary of V_r values for COF-EO$_x$/PAN).

(*SI Appendix*, Fig. S17). Interestingly, the experimentally determined channel sizes for the COF membranes embedded with oligoethers were found to be much bigger than those calculated using Zeo++ software, which provided values of 2.25, 1.57, 1.23, 1.20, and 0.71 nm for COF-EO_0, COF-EO_1, COF-EO_2, COF-EO_3, and COF-EO_4, respectively (*SI Appendix*, Table S2). Moreover, the discrepancy between the experimental and calculated values increased with the length of the oligoether chain. This trend suggests that oligoether chains have high flexibility in the presence of solvent, particularly water, leading to an increase in the effective pore size of the COF membranes. To delve deeper into the dynamics of oligoether chains, ab initio MD simulations were conducted. These simulations revealed that the oligoether chains oscillate within the membrane channels, a motion likely driven by hydrogen bonding interactions between the water molecules and oligoether chains, along with the motion of the water molecules themselves. This hypothesis is reinforced by FT-IR spectroscopy, where we observed a blue shift in the C–O stretching frequency following the addition of water (29) (*SI Appendix*, Figs. S18 and S19 and Movie S1).

Investigation of Li^+ and Mg^{2+} Transmembrane Permeability. After confirming the successful fabrication of the COF membranes, we measured their reversal potentials to investigate the influence of the number of EO units on ion permeability. For this purpose, a membrane was assembled between two conductive cells, with the side facing the COF active layer referred to as the *cis* side and the other side as the *trans* side (*SI Appendix*, Fig. S20). To assess the relative permeability of Li^+ and Mg^{2+}, the concentration of anions was maintained the same, with 0.05 M $MgCl_2$ solution on the *cis* side and 0.1 M LiCl solution on the *trans* side. Current–voltage (I–V) curves were recorded using a pair of Ag/AgCl electrodes. Significant variations in the reversal potentials (V_r, x-intercepts of the I–V curves) were detected for the COF-EO_x membranes, confirming that the number of EO units has an impact on ion permeability (30) (Fig. 3*C*). Notably, a distinct volcano-like curve was observed for the relative permeabilities of Li^+ and Mg^{2+} as a function of the number of EO units (Fig. 3 *C*, *Inset*). The COF-EO_2/PAN membrane, with a moderate length of oligoether chains, exhibited the largest discrepancy in the relative transport rates of Li^+ and Mg^{2+} ions. This finding aligns well with the results obtained from MD simulations.

Given these differences, we hypothesized that COF-EO_x/PAN membranes would lead to distinct separation outcomes for Li^+ and Mg^{2+}. To quantify the impact of the oligoether chains on the self-diffusion of Li^+ and Mg^{2+} ions, we initially measured the ion permeability of COF-EO_x/PAN under single-salt conditions and compared the data with those obtained for COF-EO_0/PAN, which lacked explicit solid-ion solvation arms. Our findings clearly indicate that increasing the length of the oligoether chains enhances ion transport, as the permeability increases with an increasing number of EO units (Fig. 4*A* and *SI Appendix*, Figs. S21–S25). Notably, COF-EO_4/PAN, containing four EO units, exhibited the highest ionic permeability for both Li^+ and Mg^{2+} ions, surpassing the permeability of COF-EO_1/PAN by more than two orders of magnitude. It is worth noting that while the pore sizes of these membranes slightly decreased with increasing oligoether length, these results provide confirmatory evidence regarding the facilitative role of the embedded oligoether chains in promoting ion transport.

To rationalize these experimental observations, we conducted an analysis of the concentrations of Li^+ and Mg^{2+} ions within COF-EO_x/PAN by measuring their transmembrane conductances under symmetric salt conditions at concentrations ranging from 10^{-5} to 1 M. We found that the normalized ion conductivities deviated from the bulk values for both Li^+ and Mg^{2+} ions, with a more pronounced deviation as the length of the oligoether

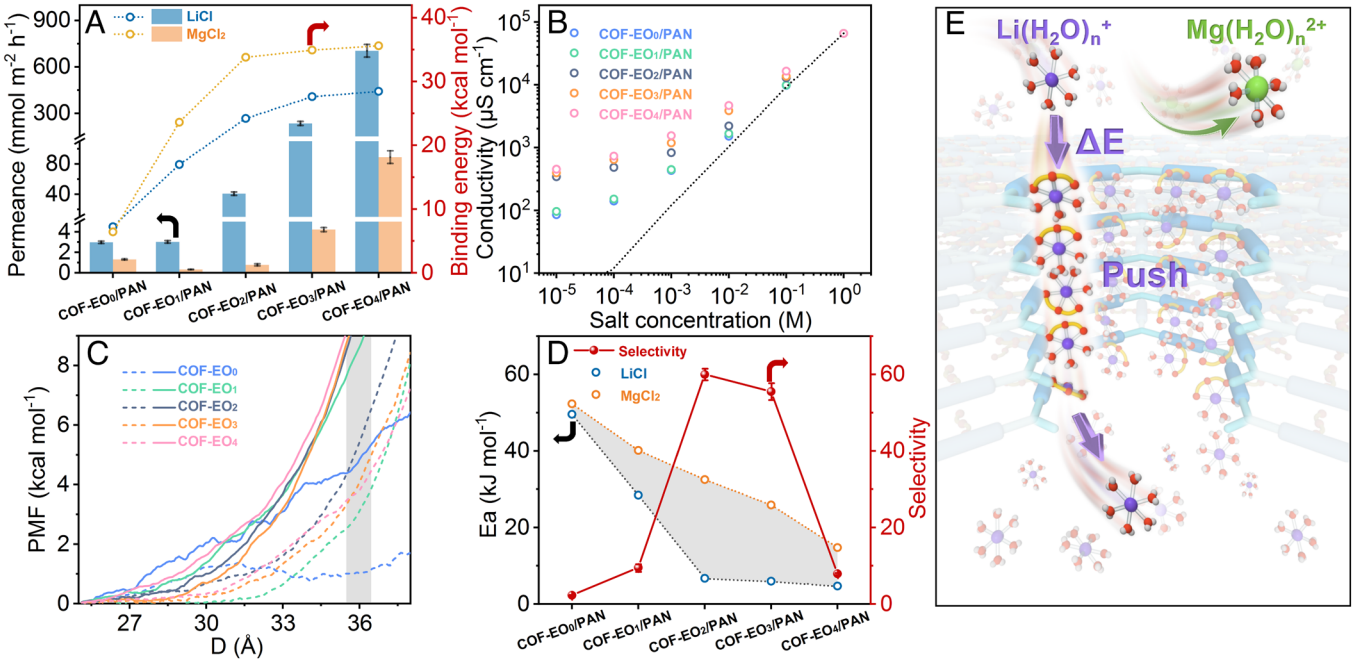

Fig. 4. (*A*) Permeance of LiCl and $MgCl_2$ across COF-EO_x/PAN tested under 1 M single-salt conditions, and binding energy of Li^+ and Mg^{2+} with the COF-EO_x derived from the DFT calculations, (*B*) conductivity versus LiCl concentration for COF-EO_x/PAN, (*C*) PMF profiles for Li^+ (dashed line) and Mg^{2+} (solid line) across COF-EO_x derived from MD calculations (gray background represents the region for ion entrance the COF pore channels and the complete PMF profiles please refers *SI Appendix*, Fig. S1), (*D*) LiCl and $MgCl_2$ transmembrane activation energies across the COF-EO_x/PAN membranes and the corresponding Li^+/Mg^{2+} selectivity tested under 1 M single-salt conditions, and (*E*) schematic of ion partitioning, conduction, and the Li^+ over Mg^{2+} selectivity across COF-EO_2/PAN. For clarity, only a portion of the outer layer of coordinated water molecules is depicte.

moieties increased (Fig. 4*B* and *SI Appendix*, Fig. S26). This suggests that membrane channels with longer oligoether chains concentrate a higher number of Li^+ and Mg^{2+} ions. Furthermore, within a specific COF membrane, the conductivity of Li^+ ions exceeded that of Mg^{2+} ions. We envisioned that by increasing the length of the polar oligoether chains leads to an elevation in the dielectric constant of the pore channel. This, in turn, enhances the ability of the pore channels to coordinate with ions, resulting in reduced resistance during ion partitioning. This behavior is analogous to ion-exchange membranes, where electrostatic interactions between ions and oppositely charged sites on the membrane compensate for the loss of the hydration shell and facilitate ion transport (31).

To qualitatively assess the process of ion dehydration, we calculated the radial distribution function (RDF) between the ions and water. By analyzing the number of peaks in the RDF, we determined that hydrated ions consist of two layers, with dehydration primarily occurring in the outer layer. The integral peak area of the RDF confirmed that Li^+ ions lose 1.5, 2.4, 2.6, 2.7, and 2.7 coordinated water molecules when passing through COF-EO_x/PAN membranes (where x = 1,2,3,4), whereas negligible water loss was observed for the COF-EO_0/PAN membrane (*SI Appendix*, Fig. S27 and Table S3). Based on these observations, we proposed that the oxygen atoms within the EO unit can act as substitutes for the water oxygen atoms that surround the ions, thereby facilitating ion transport across the membranes. However, for Mg^{2+} ions, less than one water molecule was substituted in all COF membranes (*SI Appendix*, Fig. S28). This can be attributed to the fact that ions with higher valences, such as Mg^{2+}, hold their hydration shell more tightly, resulting in greater energy resistance during partitioning from the bulk solution into the COF. Consequently, solvation interactions with oligoether moieties are less energetically favorable for Mg^{2+} ions (32).

To verify this assumption, we examined the PMF profiles, which demonstrated that the partitioning of Mg^{2+} ions into the membrane required more energy compared to Li^+ ions (Fig. 4*C* and *SI Appendix*, Fig. S1). Notably, for COF-EO_0, both Li^+ and Mg^{2+} ions exhibited smaller partitioning energies compared to COF-EO_x (x = 1,2,3,4). We believe that this is because when Li^+ and Mg^{2+} ions approached COF-EO_0, no significant dehydration was observed (33). However, the overall ion transmembrane barrier is influenced by both ion partitioning into membrane pores and diffusion across the membrane. The free energy barriers for Li^+ and Mg^{2+} ions throughout the transmembrane process showed a trend of COF-EO_0 > COF-EO_1 > COF-EO_2 > COF-EO_3 ≈ COF-EO_4 (Fig. 3*A* and *SI Appendix*, Fig. S1). This suggests that the length of the oligoether chains in COF membranes influenced ion transport, with longer chains providing greater facilitation. To gain a molecular-level understanding of how the length of the oligoether chains impacts ion transport, we employed density functional theory (DFT) calculations. The results indicated that the binding energies of COF-EO_x with Li^+ and Mg^{2+} ions increased as the length of the oligoether chains increased (Fig. 4*A* and *SI Appendix*, Fig. S29). This implies that COF membranes with longer oligoether moieties offered a more significant compensatory effect for both Li^+ and Mg^{2+} ions. To further verify this trend experimentally, we synthesized COF-EO_5/PAN, a COF membrane with five EO units on the oligoether chains (see details in *SI Appendix*, Figs. S30–S33) and examined its permeability to Li^+ and Mg^{2+} ions. As anticipated, in line with the trend described in our manuscript, the ion fluxes of COF-EO_5/PAN appeared to surpass those of COF-EO_4/PAN (*SI Appendix*, Figs. S25 and S34).

Generally, a higher ion affinity for the membrane promotes interaction but may hinder translocation. However, in our study, the greater compensating attraction between the ions and pores resulted in a higher transmembrane ion flux, deviating from conventional assumptions. To resolve this discrepancy, we conducted detailed analyses of MD trajectories, revealing that the oligoether chains exhibited flexibility, and their conformations changed during ion migration (Movie S2). While individual ions may be tightly bound to the oligoethers, the flexibility and closely spaced arrangement of the chains result in mutual repulsion. The attractive forces between the ions and the membrane pull the ions into the membrane, while the repulsive forces between the ions facilitate fast ion conduction, known as the knock-on effect. Therefore, the observed mechanisms of ion selectivity resemble those observed in biological K^+ channels (34). We assumed that although the replacement of coordinated water with the EO unit may require some energy, this coordination is beneficial for ion transport and decreases the overall transmembrane energy barriers across the entire process.

To quantitatively evaluate the transmembrane energy barriers across the COF-EO_x/PAN membranes, ion transmembrane activation energies were measured. The results revealed that transmembrane activation energies of various ions indicated that the ion transport barriers depended significantly on the length of the oligoether chains and decreased as the number of EO units increased (*SI Appendix*, Fig. S35). These results indicate that increasing the length of the oligoether chains improves the ion permeability. However, the discrepancy in the transmembrane activation energy between Li^+ and Mg^{2+} was highest for COF-EO_2, which is consistent with the MD simulations and electrochemical experimental results (Fig. 4*D*). Considering that a small energy difference alters the permeability, and thus the accompanying selectivity, we plotted these data together to establish correlations between the Li^+/Mg^{2+} separation factors and their discrepancies in the transmembrane energy barriers. A positive correlation was observed, and COF-EO_2/PAN, which exhibited the highest discrepancy in transmembrane energy barriers between Mg^{2+} and Li^+, afforded the highest Li^+/Mg^{2+} separation factor of 60 under 1 M single-salt conditions (Fig. 4*D* and *SI Appendix*, Fig. S23). These results emphasize that the observed selectivities are not characteristic of COF membranes (35–49). However, ion recognition based on coordination chemistry, which occurs via a facilitated transport mechanism, can be used to rationalize the selective separations (Fig. 4*E*). More importantly, the COF-EO_2/PAN membrane also shows excellent selectivity of Li over Na, Ca, or B, elements commonly found in salt lakes, with respective values of 1.1, 56, and 512, respectively (*SI Appendix*, Fig. S36).

Investigation of the Impact of the Density of Oligether Chains on Ion Transport and Selectivity. We proceeded to examine how the density of oligoether chains influences ion transport and selectivity. Our focus was on the COF-EO_2/PAN membrane, selected due to its superior separation capabilities. To investigate this, we employed a multivariate strategy, altering the molar ratio of Tph-EO_0 and Tph-EO_2, which are precursors for synthesizing COF-EO_0 and COF-EO_2, respectively. This led to the production of a range of membranes, termed COF-mEO_2/PAN, where "m" denotes the molar ratio of Tph-EO_2 to the sum of the two monomers used in the synthesis. The lineup included COF-0EO_2/PAN (or COF-EO_0/PAN), COF-0.33EO_2/PAN, COF-0.5EO_2/PAN, COF-0.66EO_2/PAN, COF-0.83EO_2/PAN, COF-0.92EO_2/PAN, and COF-EO_2/PAN. In 1 M single-salt conditions, we assessed the transmembrane permeability of Li^+ and Mg^{2+} ions through these membranes. A distinct pattern emerged: As the density of oligoether chains rose, there was an increase in Li^+ flux and a decrease in Mg^{2+} flux, thereby enhancing Li^+/Mg^{2+} selectivity.

For instance, the Li^+ flux in COF-EO_2/PAN was markedly higher at 41.0 mmol m^{-2} h^{-1}, compared to 3.0 mmol m^{-2} h^{-1} in COF-EO_0/PAN. The Li^+/Mg^{2+} separation factors emphasized this observation, accentuating the pivotal role of oligoether chains in boosting Li^+ transport while impeding Mg^{2+} transport (*SI Appendix*, Fig. S37).

To uncover the reasons behind the observed phenomena, we focused on the connection between the molar ratio of Tph-EO_2 to Tph-EO_0 and the resulting properties of the membranes. SEM characterization uniformly showed that all membranes maintained a consistent thickness range of 140 to 149 nm, confirming that the effects we observed were not influenced by variations in membrane thickness or compactness (*SI Appendix*, Figs. S38–S43). Our analysis further extended to IR, where we gathered semi-quantitative data on the composition of the COF-xEO_2/PAN membranes. The analysis highlighted a notable correlation between the increasing Tph-EO_2 feed ratio and the characteristic peak area of the C–O bond (1,149 to 1,120 cm^{-1}). Interestingly, we found that the actual density of oligoether chains in the membranes was significantly lower than their respective feed ratios, illustrating a complex dynamic in the synthesis process. For instance, the oligoether chain density in COF-0.92EO_2/PAN was only 68% of what the feed ratio suggested (*SI Appendix*, Fig. S44). This underlines a propensity for Tph-EO_0, which has less steric hindrance, to more readily undergo polymerization with Tp. To further examine the impact of oligoether chain proximity, we synthesized COF-0.96EO_2/PAN. This membrane demonstrated a higher Li^+ flux of 28.5 mmol m^{-2} h^{-1} and an improved Li^+/Mg^{2+} separation ratio of 40.3, underscoring the significance of the spatial arrangement of oligoether chains in facilitating efficient Li^+-ion transport.

Investigation of Li^+/Mg^{2+} Separation Performance under Binary Salt Conditions. To evaluate the separation performance of the COF-EO_x/PAN membranes under practical conditions, diffusion experiments were performed using binary feed solutions containing equal Li^+ and Mg^{2+} ion concentrations (0.025 to 1 M). The peak binary salt selectivity for Li^+ over Mg^{2+} ions ranged from 15 to 331 (Fig. 5*A* and *SI Appendix*, Figs. S45–S48). The higher Li^+/Mg^{2+} selectivity of COF-EO_x/PAN tested under binary conditions, compared to single-salt conditions, can be attributed to the considerably reduced fluxes of Mg^{2+} ions under binary conditions owing to competitive binding. To quantitatively analyze this phenomenon, the ion fluxes in the binary systems were normalized to those observed in single-salt solutions. This analysis revealed that the flux of Li^+ and Mg^{2+} ions under binary conditions decreased by 0.34 to 0.60 and 0.06 to 0.19, respectively. Consequently, the increased Li^+/Mg^{2+} selectivity can be inferred (Fig. 5*B*). The permeability of Mg^{2+} ions decreased more under binary-salt conditions because the energy was unfavorable for its partitioning. The decreased permeability of Li^+ ions can be rationalized by the dielectric effect, as evidenced by the fact that the reduced flux of Li^+ ions persisted even without $MgCl_2$ in the feed solution as long as the membrane was pretreated with Mg^{2+} ions (50) (*SI Appendix*, Fig. S49). This was because the adsorbed Mg^{2+} ions established a membrane potential that reduced the cation flux.

Investigation of Li^+/Mg^{2+} Separation Performance under Electro-Driven Binary-Salt Conditions. To investigate the practical applications of COF-EO_x/PAN, we assessed its performance under electro-driven conditions using a setup similar to that of an industrial electrodialysis cell, with a current density of 5 mA cm^{-2} (*SI Appendix*, Fig. S50). A binary aqueous solution containing 0.1 M LiCl/0.1 M $MgCl_2$ was utilized for the experiments. For comparison, we also evaluated the ion separation capability of a state-of-the-art commercial ion-exchange membrane, known as ASTOM. The COF membranes exhibited an anomalous Li^+/Mg^{2+} separation factor that varied with the number of EO units on the oligoether chains. Despite the significantly increased ion permeability observed under electro-driven conditions, we achieved a remarkable Li^+/Mg^{2+} separation factor of 1352. This value significantly exceeded those obtained under optimized dialysis conditions for COF-EO_2/PAN, positioning it among the top-performing systems reported to date (14, 51–63) (Fig. 5*C* and *SI Appendix*, Fig. S51 and Table S4). It is important to note that the separation factor after 3 h was calculated because the concentration of Mg^{2+} fell below the detection limit of the ion chromatography after 2 h. The significantly improved selectivity of COF-EO_2/PAN under electro-driven conditions can be attributed to the heightened competitive interaction between Li^+ and Mg^{2+}. Moreover, the Li^+/Mg^{2+} selectivity of COF-EO_2/PAN surpasses that of ASTOM by over two orders of magnitude. Consequently, the mole ratio of Li^+/Mg^{2+} increased substantially from 0.06 to 10.9 in the simulated West Taijinar (China) and from 0.61 to 230 in the Atacama Salar Brine (Chile) following electrodialysis using COF-EO_2/PAN (64). This demonstrates the promising potential of COF-EO_2/PAN in practical Li-extraction applications. Furthermore, COF-EO_2/PAN exhibited excellent long-term stability. Its permeability and selectivity were maintained during continuous operation under electrodialysis conditions for 4 h.

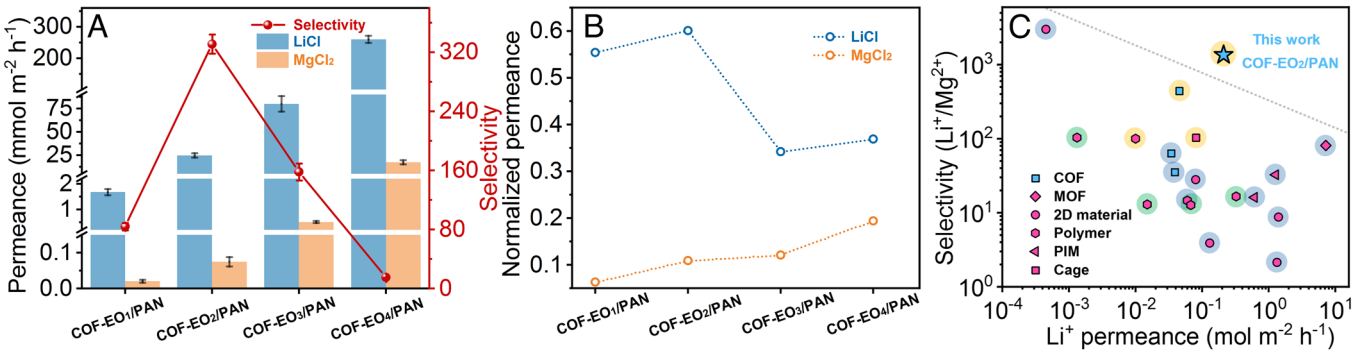

Fig. 5. (*A*) Permeance of LiCl and $MgCl_2$ and the corresponding selectivity of LiCl over $MgCl_2$ across COF-EO_x/PAN tested under binary salt conditions (1 M each, error bars represent the SDs of three different measurements), (*B*) normalized permeance of LiCl and $MgCl_2$ tested under binary conditions to those tested under single salt conditions (1 M each), and (*C*) comparison of Li^+/Mg^{2+} selectivity and permeance of LiCl for COF-EO_2/PAN with other benchmark membrane materials of COFs (refs. 14, 51, and 52), MOFs (ref. 53), 2D materials (refs. 54–56), polymers (refs. 57–61), PIMs (ref. 62), and cages (ref. 63). The membrane testing area for all cases exceeds 0.5 cm^2. The driving forces used in the experiments are represented by blue, green, and yellow backgrounds, corresponding to concentration, pressure, and electricity, respectively.

Although there was a slight decrease in selectivity over time, it fully recovered after the membrane was washed with deionized water for at least 10 cycles (*SI Appendix*, Fig. S52). We detected a similar trend in the Li^+/Mg^{2+} selectivity during operation for ASTOM, with the selectivity decreasing from 11.6 to 6.7 within the initial 2 to 10 h (*SI Appendix*, Fig. S53). The comprehensive stability and outstanding selectivity of COF-EO_2/PAN under various conditions position it as a promising candidate for practical Li-extraction applications. Furthermore, we observed no significant changes in the crystallinity or morphology of COF-EO_x/PAN during the recycling process, confirming its long-term operational stability (*SI Appendix*, Figs. S54–S56).

Discussion

In this study, we conducted a systematic investigation to understand how the solvating segments of oligoether chains influence the ion partitioning, diffusion, and selectivity of COF membranes. These membranes act as catalysts, facilitating ion transport through low-energy barrier pathways. We found that the replacement of hydrated water molecules with solvating segments is more energetically favorable for Li^+ compared to Mg^{2+}. As a result, the energy penalty for Li^+ during this process is smaller, leading to the observed selectivity. Furthermore, the association of Li^+ and Mg^{2+} with the densely populated oligoether chains leads to an enrichment of ions in the membrane pore channels, effectively partitioning them from the bulk solution. This enrichment promotes ion conduction through the membrane, facilitated by electrostatic repulsion. The overall selectivity of the membranes was determined by analyzing the discrepancy between the transmembrane activation energies of Li^+ and Mg^{2+}. The molecular mechanisms underlying the observed ion selectivity suggest that tailoring the ion-membrane binding energies holds promise for enhancing ion selectivity while maintaining high ion conduction. This understanding opens up avenues for optimizing COF membranes and designing materials with improved ion separation properties for various practical applications.

Materials and Methods

All reagents were commercially available and purchased in high purity and used without purification. The PAN ultrafiltration membrane, with a molecular weight cut off of 50,000 Da, was purchased from Sepro Membranes, Inc. (Carlsbad, CA, USA). PXRD patterns were collected using a Bruker AXS D8 Advance A25 Powder X-ray diffractometer (40 kV, 40 mA) using Cu Kα (λ = 1.5406 Å) radiation. SEM was performed on a Hitachi SU 8000 instrument. For high-resolution transmission electron microscope, a JEM-2100F was employed. FTIR spectra were recorded on a Nicolet Impact 410 FTIR spectrometer. ^{13}C (100.5 MHz) cross-polarization magic-angle spinning was recorded on a Varian infinity plus 400 spectrometer equipped with a magic-angle spin probe in a 4-mm ZrO_2 rotor. GIWAXS measurements were carried out using a XEUSS 3.0* instrument equipped with a high-intensity rotating anode X-ray generator, with an incident angle set at 0.2°. The samples were recorded within the 2θ range of 2 to 20°. To analyze the orientation of the COF layer, two-dimensional GIWAXS (2D-GIWAXS) was conducted employing an XEUSS SAXS/WAXS system, at an incident angle of 0.2°. For the 2D-GIWAXS measurements, membrane samples were cut into small pieces (1 cm × 1 cm) and affixed to a silicon wafer. The obtained 2D-GIWAXS data for the membranes were analyzed using a Dectris EIGER2 Si 1M detector.

Data, Materials, and Software Availability. All study data are included in the article and/or supporting information.

ACKNOWLEDGMENTS. This work was supported by the National Key Research and Development Program of China (2022YFA1503004), the NSF of China (22205198 and 22108202), and the NSF of Zhejiang province (LR23B060001, LY22B06004, and LY23B060022). We are grateful to Prof. Li Zhang from the School of Chemistry and Chemical Engineering, Zhejiang Sci-Tech University, for her valuable suggestions. Additionally, we appreciate the assistance of Fang Chen and Yayu Qiu from Analytical Testing Center of the Department of Chemistry, Zhejiang University, in conducting TEM and GIWAXS measurements.

Author affiliations: [a]Zhejiang Provincial Key Laboratory of Advanced Chemical Engineering Manufacture Technology, College of Chemical and Biological Engineering, Zhejiang University, Hangzhou 310027, China; [b]State Key Laboratory of Separation Membranes and Membrane Processes, School of Chemical Engineering and Technology, Tiangong University, Tianjin 300387, China; [c]Key Laboratory of Surface and Interface Science of Polymer Materials of Zhejiang Province, School of Chemistry and Chemical Engineering, Zhejiang Sci-Tech University, Hangzhou 310018, China; and [d]Department of Chemistry, University of North Texas, Denton, TX 76201

1. B. C. Gibb, The rise and rise of lithium. *Nat. Chem.* **13**, 107–109 (2021).
2. A. Battistel, M. S. Palagonia, D. Brogioli, F. L. Mantia, R. Trócoli, Electrochemical methods for lithium recovery: A comprehensive and critical review. *Adv. Mater.* **32**, 1905440 (2020).
3. S. Yang, F. Zhang, H. Ding, P. He, H. Zhou, Lithium metal extraction from seawater. *Joule* **2**, 1648–1651 (2018).
4. H. Vikström, S. Davidsson, M. Höök, Lithium availability and future production outlooks. *Appl. Energy* **110**, 252–266 (2013).
5. Z. Li *et al.*, Continuous electrical pumping membrane process for seawater lithium mining. *Energy Environ. Sci.* **14**, 3152–3159 (2021).
6. A. Razmjou, M. Asadnia, E. Hosseini, A. H. Korayem, V. Chen, Design principles of ion selective nanostructured membranes for the extraction of lithium ions. *Nat. Commun.* **10**, 5793 (2019).
7. R. Epsztein, R. M. DuChanois, C. L. Ritt, A. Noy, M. Elimelech, Towards single-species selectivity of membranes with subnanometre pores. *Nat. Nanotechnol.* **15**, 426–436 (2020).
8. C. R. Martin, Z. S. Siwy, Learning nature's way: Biosensing with synthetic nanopores. *Science* **317**, 331–332 (2007).
9. S. M. Iqbal, D. Akin, R. Bashir, Solid-state nanopore channels with DNA selectivity. *Nat. Nanotechnol.* **2**, 243–248 (2007).
10. S. J. Warnock *et al.*, Engineering Li/Na selectivity in 12-crown-4–functionalized polymer membranes. *Proc. Natl. Acad. Sci. U.S.A.* **118**, e2022197118 (2021).
11. D. A. Doyle *et al.*, The structure of the potassium channel: Molecular basis of K^+ conduction and selectivity. *Science* **280**, 69–77 (1998).
12. R. M. DuChanois *et al.*, Designing polymeric membranes with coordination chemistry for high-precision ion separations. *Sci. Adv.* **8**, eabm9436 (2022).
13. S. Bing *et al.*, Bio-inspired construction of ion conductive pathway in covalent organic framework membranes for efficient lithium extraction. *Matter* **4**, 2027–2038 (2021).
14. L. A. Richards, A. I. Schäfer, B. S. Richards, B. Corry, The importance of dehydration in determining ion transport in narrow pores. *Small* **8**, 1701–1709 (2012).
15. S. Sahu, M. D. Ventra, M. Zwolak, Dehydration as a universal mechanism for ion selectivity in graphene and other atomically thin pores. *Nano Lett.* **17**, 4719–4724 (2017).
16. B. Tansel, Significance of thermodynamic and physical characteristics on permeation of ions during membrane separation: Hydrated radius, hydration free energy and viscous effects. *Sep. Purif. Technol.* **86**, 119–126 (2012).
17. Q. Xu, S. Tao, Q. Jiang, D. Jiang, Ion conduction in polyelectrolyte covalent organic frameworks. *J. Am. Chem. Soc.* **140**, 7429–7432 (2018).
18. G. Zhang *et al.*, Accumulation of glassy poly(ethylene oxide) anchored in a covalent organic framework as a solid-state Li^+ electrolyte. *J. Am. Chem. Soc.* **141**, 1227–1234 (2019).
19. M. J. Strauss *et al.*, Lithium-conducting self-assembled organic nanotubes. *J. Am. Chem. Soc.* **143**, 17655–17665 (2021).
20. Z. Guo *et al.*, Fast ion transport pathway provided by polyethylene glycol confined in covalent organic frameworks. *J. Am. Chem. Soc.* **141**, 1923–1927 (2019).
21. Z. Xie *et al.*, Stable 2D heteroporous covalent organic frameworks for efficient ionic conduction. *Angew. Chem. Int. Ed. Engl.* **58**, 15742–15746 (2019).
22. S. Kandambeth *et al.*, Construction of crystalline 2D covalent organic frameworks with remarkable chemical (acid/base) stability via a combined reversible and irreversible route. *J. Am. Chem. Soc.* **134**, 19524–19527 (2012).
23. C. Sun *et al.*, High aspect ratio nanotubes assembled from macrocyclic iminium salts. *Proc. Natl. Acad. Sci. U.S.A.* **115**, 8883–8888 (2018).
24. T. Huang *et al.*, Single solution-phase synthesis of charged covalent organic framework nanosheets with high volume yield. *Angew. Chem. Int. Ed. Engl.* **62**, e202209306 (2023).
25. H. Wang *et al.*, Covalent organic framework membranes for efficient separation of monovalent cations. *Nat. Commun.* **13**, 7123 (2022).
26. C. Kang *et al.*, Insertion of CO_2 in metal ion-doped two-dimensional covalent organic frameworks. *Proc. Natl. Acad. Sci. U.S.A.* **120**, e2217081120 (2023).
27. A. Esfandiar *et al.*, Size effect in ion transport through angstrom-scale slits. *Science* **358**, 511–513 (2017).
28. B. Cheng, Y. Zhong, Y. Qiu, S. Vaikuntanathan, J. Park, Giant gateable osmotic power generation from a goldilocks two-dimensional polymer. *J. Am. Chem. Soc.* **145**, 5261–5269 (2023).
29. B. A. Rogers *et al.*, Weakly hydrated anions bind to polymers but not monomers in aqueous solutions. *Nat. Chem.* **14**, 40–45 (2022).
30. W.-L. Huang, X.-D. Wang, Y.-F. Ao, Q.-Q. Wang, D.-X. Wang, Artificial chloride-selective channel: Shape and function mimic of the ClC channel selective pore. *J. Am. Chem. Soc.* **142**, 13273–13277 (2020).
31. F. Xu, L. Dai, Y. Wu, Z. Xu, Li^+/Mg^{2+} separation by membrane separation: The role of the compensatory effect. *J. Membr. Sci.* **636**, 119542 (2021).

32. W. Xin *et al.*, Biomimetic KcsA channels with ultra-selective K^+ transport for monovalent ion sieving. *Nat. Commun.* **13**, 1701 (2022).
33. R. M. DuChanois, C. J. Porter, C. Violet, R. Verduzco, M. Elimelech, Membrane materials for selective ion separations at the water–energy nexus. *Adv. Mater.* **33**, 2101312 (2021).
34. W. Kopec *et al.*, Direct knock-on of desolvated ions governs strict ion selectivity in K^+ channels. *Nat. Chem.* **10**, 813–820 (2018).
35. S. Zhao *et al.*, Hydrophilicity gradient in covalent organic frameworks for membrane distillation. *Nat. Mater.* **20**, 1551–1558 (2021).
36. M. Wang *et al.*, Ultrafast seawater desalination with covalent organic framework membranes. *Nat. Sustain.* **5**, 518–526 (2022).
37. K. Wang *et al.*, Monolayer-assisted surface-initiated schiff–base-mediated aldol polycondensation for the synthesis of crystalline sp^2 carbon-conjugated covalent organic framework thin films. *J. Am. Chem. Soc.* **145**, 5203–5210 (2023).
38. S. Zhang *et al.*, Ultrathin membranes for separations: A new era driven by advanced nanotechnology. *Adv. Mater.* **34**, 2108457 (2022).
39. M. Wang *et al.*, Electrochemical interfacial polymerization toward ultrathin COF membranes for brine desalination. *Angew. Chem. Int. Ed. Engl.* **62**, e202219084 (2023).
40. Z. Zhang *et al.*, Cation-selective two-dimensional polyimine membranes for high-performance osmotic energy conversion. *Nat. Commun.* **13**, 3935 (2022).
41. S. Wang *et al.*, Two-dimensional nanochannel membranes for molecular and ionic separations. *Chem. Soc. Rev.* **49**, 1071–1089 (2020).
42. K. Dey *et al.*, Selective molecular separation by interfacially crystallized covalent organic framework thin films. *J. Am. Chem. Soc.* **139**, 13083–13091 (2017).
43. H. Yang, J. Xu, H. Cao, J. Wu, D. Zhao, Recovery of homogeneous photocatalysts by covalent organic framework membranes. *Nat. Commun.* **14**, 2726 (2023).
44. P. Wang *et al.*, Single-phase covalent organic framework staggered stacking nanosheet membrane for CO_2-selective separation. *Angew. Chem. Int. Ed. Engl.* **60**, 19047–19052 (2021).
45. J. Shen *et al.*, Fast water transport and molecular sieving through ultrathin ordered conjugated-polymer-framework membranes. *Nat. Mater.* **21**, 1183–1190 (2022).
46. C. Yin *et al.*, Perpendicular alignment of covalent organic framework (COF) pore channels by solvent vapor annealing. *J. Am. Chem. Soc.* **145**, 11431–11439 (2023).
47. Y. Zhang *et al.*, Molecularly soldered covalent organic frameworks for ultrafast precision sieving. *Sci. Adv.* **7**, eabe8706 (2021).
48. Y. Li *et al.*, Laminated self-standing covalent organic framework membrane with uniformly distributed subnanopores for ionic and molecular sieving. *Nat. Commun.* **11**, 599 (2020).
49. A. Knebel, J. Caro, Metal–organic frameworks and covalent organic frameworks as disruptive membrane materials for energy-efficient gas separation. *Nat. Nanotechnol.* **17**, 911–923 (2022).
50. A. E. Yaroshchuk, Dielectric exclusion of ions from membranes. *Adv. Colloid Interface Sci.* **85**, 193–230 (2000).
51. F. Sheng *et al.*, Efficient ion sieving in covalent organic framework membranes with sub-2-nanometer channels. *Adv. Mater.* **33**, 2104404 (2021).
52. L. Hou *et al.*, Understanding the ion transport behavior across nanofluidic membranes in response to the charge variations. *Adv. Funct. Mater.* **31**, 2009970 (2021).
53. R. Xu, Y. Kang, W. Zhang, X. Zhang, B. Pan, Oriented UiO-67 metal–organic framework membrane with fast and selective lithium-ion transport. *Angew. Chem. Int. Ed. Engl.* **60**, e202115443 (2021).
54. L. Ding *et al.*, Effective ion sieving with $Ti_3C_2T_x$ MXene membranes for production of drinking water from seawater. *Nat. Sustain.* **3**, 296–302 (2020).
55. C. E. Ren *et al.*, Charge- and size-selective ion sieving through $Ti_3C_2T_x$ MXene membranes. *J. Phys. Chem. Lett.* **6**, 4026–4031 (2015).
56. Z. Lu, Y. Wu, L. Ding, Y. Wei, H. Wang, A lamellar MXene ($Ti_3C_2T_x$)/PSS composite membrane for fast and selective lithium-ion separation. *Angew. Chem. Int. Ed. Engl.* **60**, 22265–22269 (2021).
57. Q. Wen *et al.*, Highly selective ionic transport through subnanometer pores in polymer films. *Adv. Funct. Mater.* **26**, 5796–5803 (2016).
58. H. Peng, Q. Zhao, A nano-heterogeneous membrane for efficient separation of lithium from high magnesium/lithium ratio brine. *Adv. Funct. Mater.* **31**, 2009430 (2021).
59. H. Wu *et al.*, Positively-charged PEI/TMC nanofiltration membrane prepared by adding a diamino-silane coupling agent for Li^+/Mg^{2+} separation. *J. Membr. Sci.* **672**, 121468 (2023).
60. Q. Li *et al.*, High performance Li^+/Mg^{2+} separation membrane by grafted short chain amino-rich monomers. *J. Membr. Sci.* **677**, 121634 (2023).
61. W. Li *et al.*, A positively charged composite nanofiltration membrane modified by EDTA for LiCl/$MgCl_2$ separation. *Sep. Purif. Technol.* **186**, 233–242 (2017).
62. R. Tan *et al.*, Hydrophilic microporous membranes for selective ion separation and flow-battery energy storage. *Nat. Mater.* **19**, 195–202 (2020).
63. T. Xu *et al.*, Highly ion-permselective porous organic cage membranes with hierarchical channels. *J. Am. Chem. Soc.* **144**, 10220–10229 (2022).
64. L. Wu *et al.*, Lithium recovery using electrochemical technologies: Advances and challenges. *Water Res.* **221**, 118822 (2022).